Reprinted from

JAPANESE JOURNAL OF
APPLIED
PHYSICS

REGULAR PAPER

Detection of Arterial Wall Boundaries Using an Echo Model Composed of Multiple Ultrasonic Pulses

Nabilah Ibrahim, Hideyuki Hasegawa, and Hiroshi Kanai

Jpn. J. Appl. Phys. **52** (2013) 07HF03

Japanese Journal of Applied Physics **52** (2013) 07HF03 **REGULAR PAPER**
http://dx.doi.org/**10.7567/JJAP.52.07HF03**

Detection of Arterial Wall Boundaries Using an Echo Model Composed of Multiple Ultrasonic Pulses

Nabilah Ibrahim[1], Hideyuki Hasegawa[2,1], and Hiroshi Kanai[1,2*]

[1]*Graduate School of Engineering, Tohoku University, Sendai 980-8579, Japan*
[2]*Graduate School of Biomedical Engineering, Tohoku University, Sendai 980-8579, Japan*
E-mail: kanai@ecei.tohoku.ac.jp

Received November 20, 2012; accepted March 27, 2013; published online June 20, 2013

The assessment of the intima-media thickness (IMT) of the carotid arterial wall, which is the most frequently used indicator to diagnose atherosclerosis by ultrasound, involves the measurement of the lumen-intima boundary (LIB) and media-adventitia boundary (MAB). In this study, using the mean squared error (MSE) method and by applying the template matching technique, an adaptive model of an ultrasonic echo, which is obtained from an ultrasonic pulse measured with a hydrophone, was fitted with the measured in vivo RF echo to estimate the boundaries of the carotid arterial wall. In the present study, the frequency and phase of the adaptive model were considered to improve the accuracy in the determination of the LIB and MAB. For a 7.5-mm-long short segment of the carotid artery in the longitudinal direction, the average IMTs estimated by the improved technique and the previous method were 502 ± 61 and $558 \pm 120\,\mu m$, respectively, showing a decrease in the standard deviation by the proposed method. Moreover, the result obtained by the improved technique presented only 0.4% difference between the automatically detected boundary and the manually detected boundary, which is smaller than that obtained by the previous method (10.7% difference). These results verified that the boundary detected by the improved technique was more accurate than that detected by the previous method.

1. Introduction

Cardiovascular diseases remain the biggest cause of death worldwide. It is reported that such diseases are responsible for over 17.3 million deaths yearly and are the leading causes of death in the world.[1)] Moreover, in 2008, out of 17.3 million cardiovascular deaths, 7.3 million deaths were caused by heart attacks and 6.2 million deaths were caused by strokes or atherosclerosis. The rise in the prevalence of atherosclerosis is considered to be the main cause of cardiovascular diseases.[2–4)] Hence, assessment of the risk of atherosclerosis[5,6)] and its diagnosis at an early stage have become very important. Various noninvasive markers for detection of atherosclerosis or arterial wall alteration have been identified, such as arterial wall thickening [i.e., intima-media thickness (IMT)],[7)] endothelial dysfunction,[8)] and coronary artery calcification.[9)] Additionally, the increase of the IMT of the carotid artery, which is the region between the lumen-intima boundary (LIB) and the media-adventitia boundary (MAB), correlates very well with pathohistologic measurements for assessing cardiovascular risk.[10)] A lesion of atherosclerosis occurs when the endothelial cell lining on the luminal surface of the arterial wall is dysfunctions.[11–13)] When the cholesterol level in blood is abnormally high and the endothelium cells are injured, red blood cells become procoagulant and the adhesiveness of the blood cells increases. These responses lead to the migration of monocytes in the lumen as macrophages and the smooth-muscle cells in the media layer into the intima layer. Moreover, the accumulated macrophages swell into fat-foam cells. Consequently, those conditions increase the arterial wall thickness and narrow the blood vessel. This phenomenon is illustrated in Fig. 1. Hence, the increase in the IMT of the carotid artery is a valid surrogate marker of atherosclerosis.[14–18)] Additionally, Davis et al.[19)] have reported that the IMT measurement in the carotid artery is more reproducible than the measurement of the IMT in the abdominal aorta because there is less tissue between the ultrasonic probe and the carotid arterial wall. Furthermore,

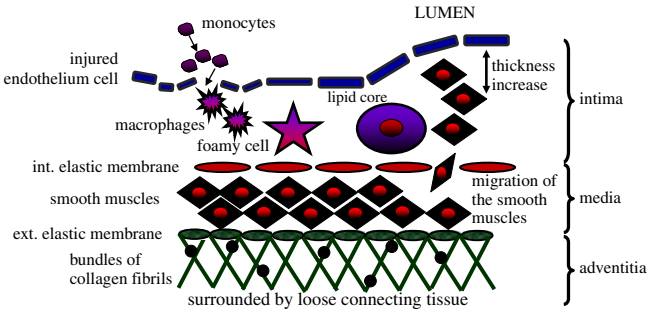

Fig. 1. (Color online) Illustration of atherosclerosis lesions in the arterial wall.

the IMT measurement is only assessed at the posterior wall of the carotid artery because of the clear double-line pattern and consistent appearance.[20–22)]

A number of methods are capable of detecting the LIB and MAB of the posterior carotid arterial wall. The manual technique for boundary detection is not a desirable method because it lacks reproducibility.[23,24)] Thus, automated techniques are necessary.[29–33)] Using the standard medical imaging tool, computed tomography (CT), cardiovascular risk factors such as hypertension and atherosclerosis have been studied,[25)] and the reproducibility of good agreement of the IMT measurement using CT with that using ultrasound has been reported.[26)] Boussel et al.[27)] and Yanai et al.[28)] compared the measurement of the IMT and thickening of the carotid arterial wall by MRI with those measured with ultrasound and found a very good agreement between these techniques. However, the method using MRI and CT is time consuming and cost ineffective compared with ultrasound. Savithri and Purushothaman[29)] estimated the arterial wall boundaries using the intensity gradient method. However, this method was significantly influenced by ultrasonic scattering in the in vivo measurement even though image enhancement, thresholding, and denoising processes were proposed. For the measurement of the IMT using the

dynamic programming method reported by Liang et al.,[30] the boundaries were detected precisely. However, the method required retraining when the image characteristics change, and is thus time consuming. Loizou et al.[31] used an active contour method for the segmentation of the carotid artery and IMT measurement in an ultrasonic image. The disadvantage of this method is that the solution often falls into the local minima rather than the global minima. This method has been reported by Rocha et al.[32] for the measurement of the boundaries using the combination of dynamic programming, intensity gradient, and active contour methods. Golemati et al.[33] used another approach by using the segmentation of a specific shape in an ultrasonic image so that the lines of the LIB and MAB could be detected. However, the method can be applied to only straight carotid arterial walls. Therefore, there is a limitation and inaccuracy in detecting random shapes or curved vessels. Hence, the accurate detection of the LIB and MAB positions is essential for the estimation of the IMT. For the accurate assessment of the LIB and MAB positions, a technique using template matching between the echo model and the measured echo is used.[34–37]

Previous efforts have been carried out to automatically assess the LIB and MAB positions using template matching between the echo models (LIB and MAB echo models) and the measured in vivo RF echoes.[34–37] The positions of the models, which give the minimum difference of the measured echo from the echo model, are determined as the LIB and MAB. The echo model is created by imitating the reference RF signal. Kaneko et al.[34] and Ikeshita et al.[35] considered the reference RF signals which is an echo from a point scatterer (wire diameter, 35 μm). However, the difference between the echo model and the measured in vivo RF echo and even that between the echo model and the reference RF signal are significant. To obtain better fitting between the echo model and the reference RF signal, the improved echo model was considered by taking the envelope signal into account and by using a Gaussian window as an envelope function of the echo model.[36] Even though the difference between the improved echo model and the reference RF signal showed a better result than the previous one,[34,35] the approach of measuring the differences between the improved echo model and the measured in vivo RF echoes did not consider the phase information and, thus, produced inadequate results. The template matching method using the envelope signal was also reported for the accurate estimation of boundaries, but it only detects the MAB.[37] Instead of creating an echo model by imitating the reference RF signal, we omit implemented the echo model by considering the estimated echo signal, which is obtained from the transmitted wave measured using a hydrophone. However, the results obtained are insufficient since the center frequencies of the echo models that need to be fitted with the measured in vivo RF echoes are fixed. A model with a fixed center frequency is not suitable because the center frequency of the echo signal from an arterial wall differs from person to person due to frequency dependent attenuation. To overcome this drawback, in the present study, the center frequency and the phase of the echo model are changed gradually to find the best fit between the echo models and the measured in vivo RF echoes. Moreover, for the accurate estimation of the MAB, the technique is improved so that the echo model could fit to the echo from the MAB instead of those from the scatterers below the adventitia layer. In addition, we showed the comparative results of detected boundaries for a few beams between our improved automated method and the previous and manual methods. In this technique, the assessment of the boundary positions is analyzed in the arterial longitudinal section of the common carotid artery because it provides a clearer description of the border between the lumen and the arterial wall. Moreover, in the longitudinal section, the averaging of the IMT over a short segment of the artery is applicable.[36]

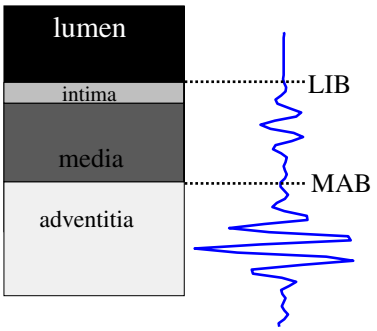

Fig. 2. (Color online) Schematic of longitudinal section of arterial wall (left) and ultrasound echo (right).

2. Principle and Methodology

Morphologically, the structure of the arterial wall consists of three layers, i.e., the intima, media, and adventitia, which enable arteries to maintain their function and strength. The very thin intima layer consists of a single layer of endothelial cells lining the luminal surface of the arterial wall, and the media layer, which is the middle layer of the artery, consists of a complex network of smooth muscle cells, elastin, and collagen fibrils. Meanwhile, the adventitia layer, which is the mechanically strong outer layer, consists mainly of fibroblasts, fibrocytes, and bundles of collagen fibrils.[38] These different characteristics of the respective layers produce a particular ultrasonic echo composed of reflected echoes from the LIB and MAB, as shown in the schematic view of the posterior wall in the longitudinal section illustrated in Fig. 2. In an echo signal from the posterior wall, an ultrasonic echo reflected from the LIB is found, followed by a slightly low amplitude region in the media, and another echo is found around the MAB. Since the distance between the LIB and the MAB, which is defined as the IMT, is considered as a valid surrogate marker of atherosclerosis, the positions of the LIB and MAB should be determined accurately. Subsequently, in the present study, using our proposed template matching, the LIB and MAB are determined automatically. First, we created the echo models for the LIB and MAB using a transmitted wave measured using a hydrophone.

2.1 Outline of proposed method

The proposed template matching technique for automatic assessment of the LIB and MAB provides the LIB and MAB echo models as the template to be matched with the measured signal from the posterior carotid arterial wall. Figure 3 shows the flow chart of the outline of the proposed

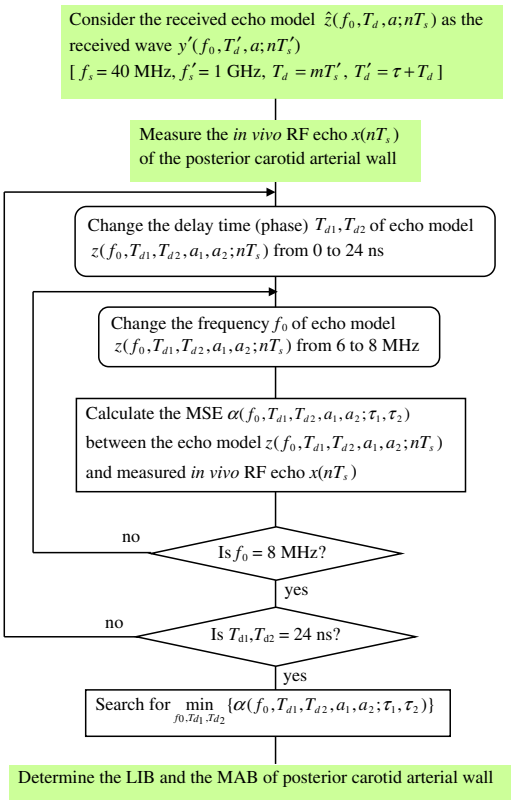

Fig. 3. (Color online) Flow chart of the outline of the proposed method to accurately detect the boundaries of the carotid arterial wall.

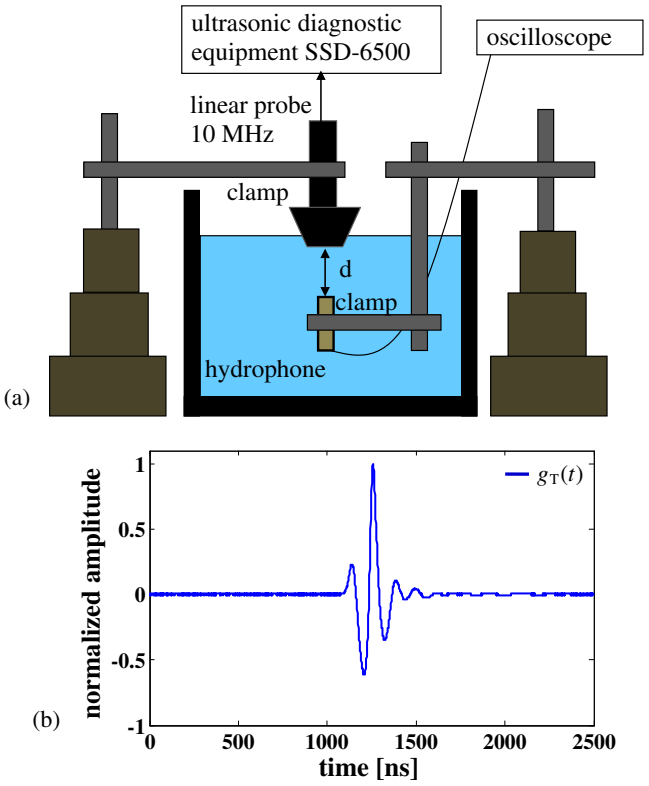

Fig. 4. (Color online) (a) Experimental setup of measuring transmitted wave using a hydrophone. (b) Transmitted wave measured using a hydrophone.

method. In the beginning, a model $\hat{z}(f_0, T_\mathrm{d}, a; nT_\mathrm{s})$ of a received ultrasonic pulse was implemented using a received ultrasonic pulse $y'(f_0, T_\mathrm{d}', a; nT_\mathrm{s}')$ estimated from the transmitted wave measured using a hydrophone and sampled at a much higher sampling frequency, where f_0 is the center frequency, a is the amplitude coefficient, T_s and T_s' are the sampling periods ($T_\mathrm{s} > T_\mathrm{s}'$), and T_d and T_d' correspond to the initial phases of $\hat{z}(f_0, T_\mathrm{d}, a; nT_\mathrm{s})$ and $y'(f_0, T_\mathrm{d}', a; nT_\mathrm{s}')$, respectively. Since the LIB and MAB echo models, $\hat{z}_1(f_0, T_{\mathrm{d}1}, a_1; nT_\mathrm{s})$ and $\hat{z}_2(f_0, T_{\mathrm{d}2}, a_2; nT_\mathrm{s})$, are being utilized to determine the boundaries, the optimum echo models that fit well with the measured signal $x(nT_\mathrm{s})$ are desired. The echo model $z(f_0, T_{\mathrm{d}1}, T_{\mathrm{d}2}, a_1, a_2; nT_\mathrm{s})$ is defined as the sum of $\hat{z}_1(f_0, T_{\mathrm{d}1}, a_1; nT_\mathrm{s})$ and $\hat{z}_2(f_0, T_{\mathrm{d}2}, a_2; nT_\mathrm{s})$. To obtain the optimum echo model, the center frequency f_0 of the echo model $z(f_0, T_{\mathrm{d}1}, T_{\mathrm{d}2}, a_1, a_2; nT_\mathrm{s})$ is changed gradually from 6 to 8 MHz and the root-mean-squared differences $\alpha(f_0, T_{\mathrm{d}1}, T_{\mathrm{d}2}, a_1, a_2; \tau_1, \tau_2)$ between the echo model $z(f_0, T_{\mathrm{d}1}, T_{\mathrm{d}2}, a_1, a_2; nT_\mathrm{s})$ and the measured in vivo RF echo $x(nT_\mathrm{s})$ are estimated using the mean squared error (MSE) method, where τ_i and a_i are the time delay and amplitude coefficient of the LIB and MAB echo models, respectively ($i = 1$: LIB, 2: MAB). The phases of the echo models are also changed by changing time delay $T_{\mathrm{d}1}, T_{\mathrm{d}2}$ at a pitch of T_s' [$= 1/f_\mathrm{s}', f_\mathrm{s}'$: sampling frequency of estimated received pulse $y'(f_0, T_\mathrm{d}', a; nT_\mathrm{s}')$]. Afterwards, the minimum difference $\min\{\alpha(f_0, T_{\mathrm{d}1}, T_{\mathrm{d}2}, a_1, a_2; \tau_1, \tau_2)\}$ is searched to accomplish the best fit between the echo models and the measured in vivo RF echo. The positions of the models for LIB and MAB echoes are determined as the boundaries of LIB and MAB of the posterior carotid arterial wall.

2.2 Measurement of received ultrasonic pulse used for creation of echo model

In this study, an echo model $z(f_0, T_{\mathrm{d}1}, T_{\mathrm{d}2}, a_1, a_2; nT_\mathrm{s})$ is matched with the measured in vivo RF echo $x(nT_\mathrm{s})$ from the posterior carotid arterial wall by evaluating the differences $\alpha(f_0, T_{\mathrm{d}1}, T_{\mathrm{d}2}, a_1, a_2; \tau_1, \tau_2)$ between them using the MSE method. To reduce the differences between the echo model and the measured in vivo RF echo, we implemented a received echo model $\hat{z}(f_0, T_\mathrm{d}, a; nT_\mathrm{s})$, which considered a received ultrasonic pulse $y'(f_0, T_\mathrm{d}', a; nT_\mathrm{s}')$ calculated from a transmitted wave measured using a hydrophone. A schematic of the experimental setup for the measurement of a transmitted wave using a hydrophone and the measured transmitted wave are shown in Figs. 4(a) and 4(b), respectively. The transmitted wave $g_\mathrm{T}(t)$ was emitted in a water tank with a linear-array transducer at 10 MHz (ALOKA UST-5410), which is connected to a modified ultrasonic diagnosis system (ALOKA SSD-6500). The wave was measured with a hydrophone (FORCE MHA9-150) placed at the distance d of 13.7 mm, associated with the focal distance. The wave was averaged 64 times, and recorded by a digital oscilloscope (Tektronix TDS 2014) at a sampling frequency of 1 GHz at 8-bit resolution. Figures 5(a) and 5(b) show a schematic of the propagation of the transmitted and reflected waves and the block diagram of the process that motivates the creation of a model of a received pulse using a transmitted wave, respectively. In the present study, the transfer function from an excitation signal to ultrasound in transmission and that from ultrasound to a received signal in receiving were assumed to be the same. The transmitted wave is assumed as a one-way propagation wave with

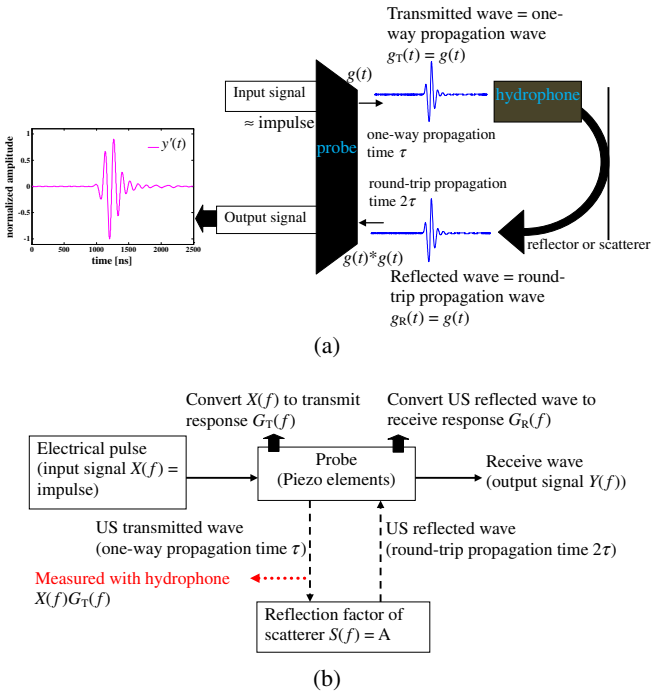

Fig. 5. (Color online) (a) Schematic propagation of transmitted and reflected waves. (b) Frequency-domain block diagram of the process that occurs when the transmitted wave encounters a scatterer.

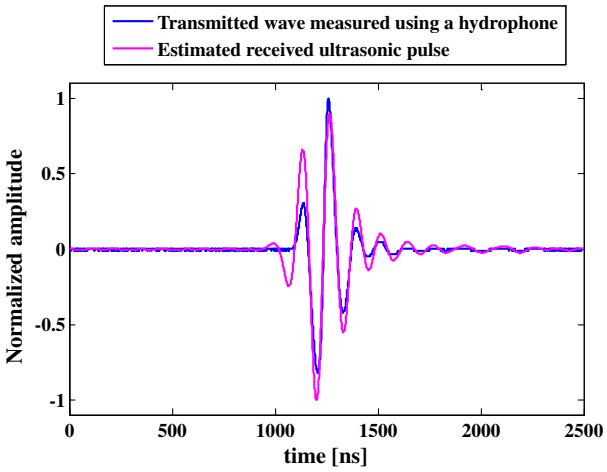

Fig. 6. (Color online) Transmitted wave measured $g_T(t)$ using a hydrophone and the estimated received ultrasonic pulse $y'(t)$.

the delay τ and the reflected wave is assumed as a round-trip propagation wave with the propagation time of 2τ [Fig. 5(a)]. From the frequency domain block diagram shown in Fig. 5(b), the process starts with the electrical signal $x(t)$ that excites the piezo elements. In the ultrasonic diagnosis equipment used in the present study, the excitation signal is a rectangular pulse with a width of half the wavelength. However, the excitation signal was assumed to be an impulse for simplicity. The piezo elements transform it to the transmitted wave $g_T(t)$. At this stage, the transmitted wave is measured using the hydrophone. Note that the wave encounters the scatterer and returns to the transducer as a reflected wave $Ag_T(t)$ with a reflection factor $S(f) = A$ (A: real constant) when a scatterer is placed along propagation path of the transmitted wave. In this process, the reflection factor $S(f)$ is assumed not to change with frequency. The reflected wave $Ag_T(t)$ that returns to the same transducer is transformed again by piezo elements, whose response is $g_R(t)$, to the received wave $y(t) = Ag_T(t) * g_R(t)$, where $*$ denotes convolution. Since the transmitting and receiving elements are the same, $g_T(t) = g_R(t)$ is appropriate. Thus, the received wave (output) $y(t)$ of the overall process can be written as

$$Y(f) = \{G_T(f)X(f)G_R(f)S(f)\} \cong A\{G(f)\}^2, \quad (1)$$

where $Y(f)$, $G_R(f)$, $G_T(f)$, and $X(f)$ are the frequency spectra of $y(t)$, $g_R(t)$, $g_T(t)$, and $x(t)$, respectively. In this work, the time delay due to the round-trip propagation of the received wave is modified to be the same as the time delay due to the one-way propagation of the transmitted wave of τ, so as to observe the transmitted wave and the received wave at the same time. Therefore, the received wave, namely the received ultrasonic pulse $y'(t)$, is defined as

$$Y'(f) = \{G_T(f)X(f)G_R(f)S(f)\}e^{j2\pi f\tau} \cong A\{G(f)\}^2 e^{j2\pi f\tau}. \quad (2)$$

To account for the received ultrasonic pulse $y'(t)$ in the time domain, the inverse Fourier transform $\Im^{-1}[\cdot]$ is applied to $Y'(f)$. Figure 6 shows the transmitted wave $g_T(t)$ measured using a hydrophone and the estimated received ultrasonic pulse $y'(t)$. The echo model that was created by referring to an echo from a point scatterer (wire diameter, 35 μm)[34,35] and a glass plate[36] is not desired because such echoes depend on the reflector, and thus the echo from the carotid arterial wall is not suitable to be fitted with. Therefore, in the present study, the received ultrasonic pulse was estimated using the transmitted wave measured using a hydrophone.

2.3 Implementation of optimum received echo model

In the subsequent sections, we have elaborated the drawback of the previous method, i.e., the results obtained are insufficient since the center frequency of the echo model, which needs to be fitted with the measured in vivo RF echoes, is fixed. Thus, in the present study, to find the best fit between the echo model $z(f_0, T_{d1}, T_{d2}, a_1, a_2; nT_s)$ and the measured in vivo RF echo $x(nT_s)$, the optimum echo model is implemented by changing the center frequency f_0 and the phases T_{d1}, and T_{d2} of the echo model gradually. As noted, an echo model $z(f_0, T_{d1}, T_{d2}, a_1, a_2; nT_s)$ is defined as the sum of LIB and MAB echo models, $\hat{z}_1(f_0, T_{d1}, a_1; nT_s)$ and $\hat{z}_2(f_0, T_{d2}, a_2; nT_s)$, and the received echo model $\hat{z}(f_0, T_d, a; nT_s)$ is determined from the received ultrasonic pulse $y'(f_0, T'_d, a; nT'_s)$. As shown in Fig. 7, the leading edge of $\hat{z}(f_0, T_d, a; nT_s)$ is determined at the zero phase of $y'(f_0, T'_d, a; nT'_s)$ with the prior length of τ. In addition, the variables T_d and T'_d are expressed as $T_d = mT'_s$ and $T'_d = \tau + T_d$. The received echo model $\hat{z}(f_0, T_d, a; nT_s)$, which is the received ultrasonic pulse $y'(f_0, T'_d, a; nT'_s)$ calculated from the transmitted wave $g_T(t)$ measured using a hydrophone, is sampled at $f'_s = 1$ GHz ($T'_s = 1/f'_s = 1$ ns). Meanwhile, the measured in vivo RF echo (details of the acquisition are described in Sect. 3) is sampled at $f_s = 40$ MHz (sample spacing: 25 ns). The center frequency f_c of the received echo model is 7.4 MHz, determined at the peak frequency of the power spectrum of the received

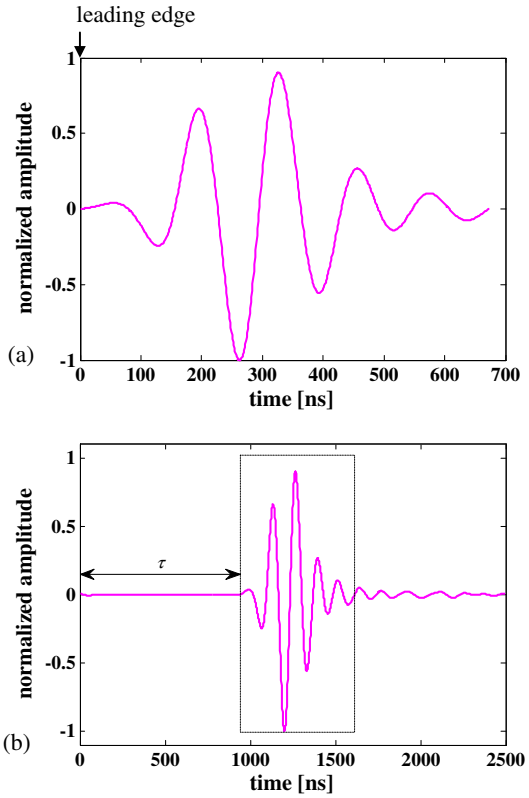

Fig. 7. (Color online) (a) Received echo model $\hat{z}(f_0, T_d, a; nT_s)$ obtained from (b) the received ultrasonic pulse $y'(T'_d, a; D_n T'_s)$.

echo model. Firstly, to obtain the same sampling interval ($1/f_s = 25$ ns) of these echo signals, even though the center frequency f_0 of the received echo model $\hat{z}(f_0, T_d, a; nT_s)$ is changed, the sampling rate T_s of the downsampled received echo model is set to be the same as the sampling rate of the measured in vivo RF echo $x(nT_s)$ of 40 MHz. By performing this procedure, the center frequency f_0 of the received echo model is changed gradually from 6 to 8 MHz at intervals of 0.3 MHz, which corresponds to one sampling interval $T_s = 1$ ns of a cycle of $f_c = 7.4$ MHz ($T_s/T'_s * f_c$). The downsampling factor D is defined as $D = f_0/f_c * T'_s/T_s$. Figures 8(b)–8(e) show the received echo models at center frequencies of 6.2, 6.5, 6.8, and 7.4 MHz at downsampling factors D of 21, 22, 23, and 25, respectively. Secondly, by changing the beginning point T_d (corresponding to the initial phase) of the received echo model $\hat{z}(f_0, T_d, a; nT_s)$ by a pitch of 1 ns, the delay time of the received echo model is changed gradually, as shown in Figs. 8(f)–8(i) for $T_d = 0$, 5, 10, and 15 ns, respectively. The difference $\alpha(f_0, T_{d1}, T_{d2}, a_1, a_2; \tau_1, \tau_2)$ between the echo model $z(f_0, T_{d1}, T_{d2}, a_1, a_2; nT_s)$ and the measured in vivo RF echo $x(nT_s)$ is calculated at the preassigned lags $\{\tau_i\}$ ($i = 1$: LIB, 2: MAB) for the received echo models at different delay times $\{T_d\}$. When the received echo model reaches the delay time of $T_d = 25$ ns, the calculation of the difference $\alpha(f_0, T_{d1}, T_{d2}, a_1, a_2; \tau_1, \tau_2)$ is repeated by incrementing the delay time $\{\tau_i\}$ by 25 ns. Therefore, the delay time T_d is changed from 0 ns to the maximum of 24 ns. Consequently, the combinations of all the center frequencies $\{f_0\}$ and the phases $\{T_d\}$ of the received echo model $\hat{z}(f_0, T_d, a; nT_s)$ could be considered to implement the optimum received echo model, and thus we are able to obtain the best fit with the measured in vivo RF echo.

2.3.1 Echo model composed of multiple received echo models obtained from received ultrasonic pulse

The optimum received echo model $\hat{z}(f_0, T_d, a; nT_s)$ is implemented by changing the center frequency and initial phase of the received echo model $y'(f_0, T'_d, a; nT'_s)$. Since the ultrasonic echo signal from the posterior wall includes mainly echoes from the LIB and MAB, as shown in Fig. 2, the echo model $z(f_0, T_{d1}, T_{d2}, a_1, a_2; nT_s)$ from the arterial wall is composed of two received echo models; the LIB and MAB echo models $\hat{z}_1(f_0, T_{d1}, a_1; nT_s)$ and $\hat{z}_2(f_0, T_{d2}, a_2; nT_s)$, which can be expressed as

$$\hat{z}(f_0, T_{d1}, T_{d1}, a_1, a_2; nT_s) = \hat{z}_1(f_0, T_{d1}, a_1; nT_s - \tau_1) + \hat{z}_2(f_0, T_{d2}, a_2; nT_s - \tau_2), \quad (3)$$

where f_0 is the center frequency, T_{d1} and T_{d2} correspond to initial phases, a_1 and a_2 are amplitude coefficients, and τ_1 and τ_2 are the time delays of the respective echoes. The parameters f_0, $\{T_{di}\}$, $\{a_i\}$, and $\{\tau_i\}$ ($i = 1$: LIB, 2: MAB) are determined so that the difference between the echo model $z(f_0, T_{d1}, T_{d2}, a_1, a_2; nT_s)$ and measured in vivo RF echo $x(nT_s)$ is minimum. Figure 9 shows the echo model $z(f_0, T_{d1}, T_{d2}, a_1, a_2; nT_s)$ composed of $\hat{z}_1(f_0, T_{d1}, a_1; nT_s)$ and $\hat{z}_2(f_0, T_{d2}, a_2; nT_s)$, at the center frequency f_0 of 7.4 MHz and the initial phases T_{d1}, and T_{d2} of 0 ns.

2.4 Procedure of fitting echo models to measured in vivo RF echo

Our proposed automated template matching method for the detection of the carotid arterial wall boundaries is realized by calculating the MSE $\alpha(f_0, T_{d1}, T_{d2}, a_1, a_2; \tau_1, \tau_2)$ between the measured in vivo RF echoes $x(nT_s)$ and the echo model $z(f_0, T_{d1}, T_{d2}, a_1, a_2; nT_s)$ expressed as

$$\begin{aligned}
&\alpha(f_0, T_{d1}, T_{d2}, a_1, a_2; \tau_1, \tau_2) \\
&= \frac{1}{N}\sum_{n=0}^{N-1} |x(nT_s) - z(f_0, T_{d1}, T_{d2}, a_1, a_2; nT_s, \tau_1, \tau_2)|^2 + \beta, \\
&= \frac{1}{N}\sum_{n=0}^{N-1} |x(nT_s) - \{\hat{z}_1(f_0, T_{d_1}, a_1; nT_s - \tau_1) \\
&\quad + \hat{z}_2(f_0, T_{d_2}, a_2; nT_s - \tau_2)\}|^2 + \beta, \\
&= \frac{1}{N}\left\{\sum_{nT_s=T_1}^{T_2} |x(nT_s) - \hat{z}_1(f_0, T_{d1}, a_1; nT_s - \tau_1)|^2 \right. \\
&\quad + \sum_{nT_s=T_3}^{T_4} |x(nT_s) - \hat{z}_2(f_0, T_{d2}, a_2; nT_s - \tau_2)|^2 \\
&\quad + \sum_{nT_s=T_2}^{T_3} |x(nT_s) - \{\hat{z}_1(f_0, T_{d1}, a_1; nT_s - \tau_1) \\
&\quad \left. + \hat{z}_2(f_0, T_{d2}, a_2; nT_s - \tau_2)\}|^2 \right\} + \beta, \qquad (4)
\end{aligned}$$

where $\{T_m\}$ ($m = 1, 2, 3, 4$) indicates the periods illustrated in Fig. 10(a) and the variance β is defined as

$$\beta = \underset{nT_s \in L_1, L_3}{\text{var}}[x(nT_s)], \qquad (5)$$

where $L_1 = \tau_1 - T_0$ and $L_3 = \tau_2 - \tau_1 - L_2$. Figure 10(a) shows an example of echo models when $\hat{z}_1(f_0, T_{d1}, a_1; nT_s)$

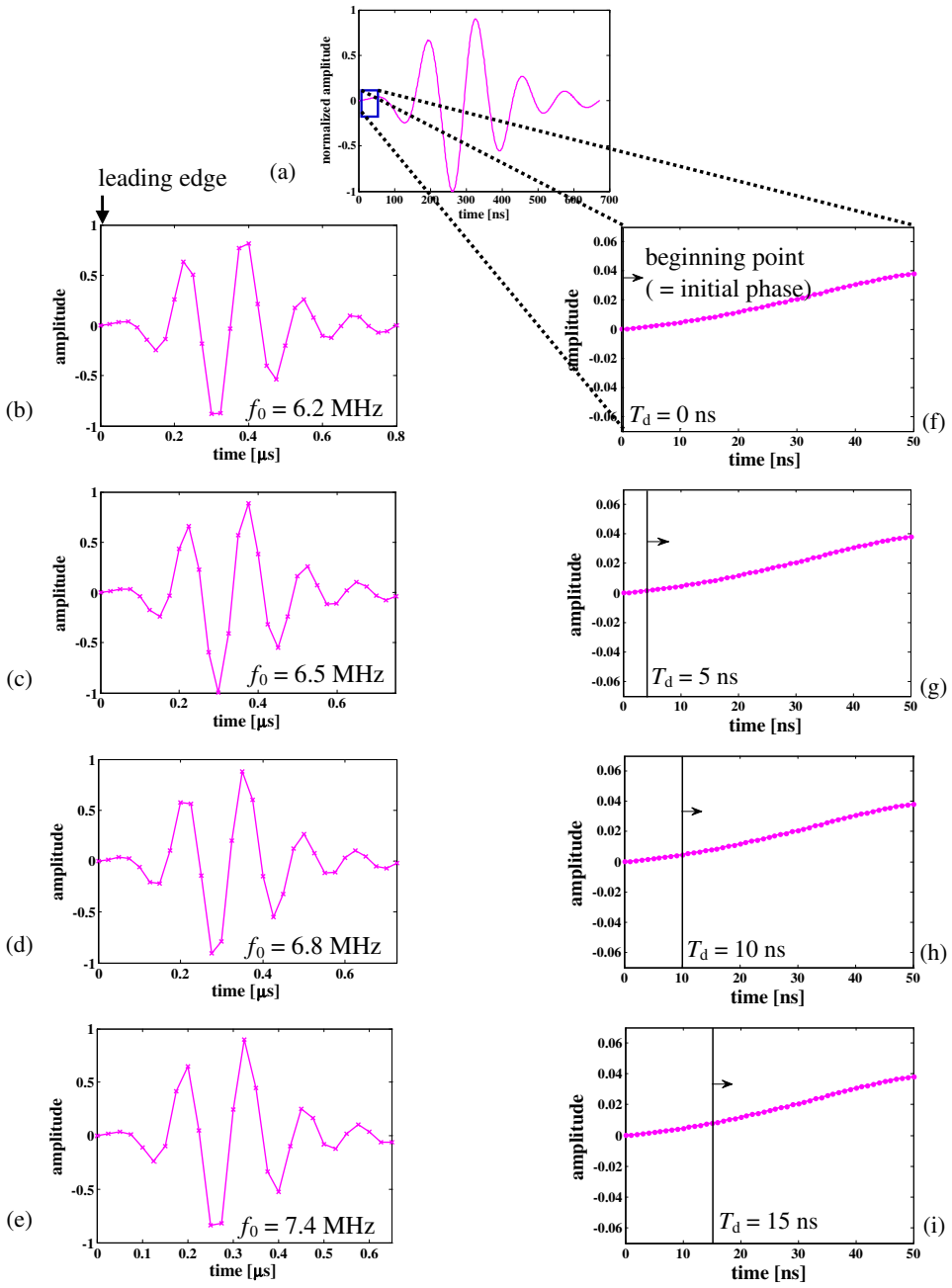

Fig. 8. (Color online) (a) Received echo model $\hat{z}(f_0, T_d, a; nT_s)$ calculated from the transmitted wave measured using a hydrophone. $\hat{z}(f_0, T_d, a; nT_s)$ at (b) $f_0 = 6.2$ MHz, (c) $f_0 = 6.5$ MHz, (d) $f_0 = 6.8$ MHz, and (e) $f_0 = 7.4$ MHz. Enlarged partial waveforms of echo model indicating the initial point of $\hat{z}(f_0, T_d, a; nT_s)$ at the delay times of (f) $T_d = 0$, (g) $T_d = 5$, (h) $T_d = 10$, and (i) $T_d = 15$ ns.

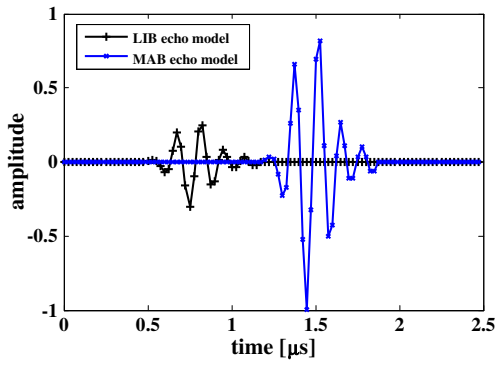

Fig. 9. (Color online) Echo model composed of LIB and MAB echo models at the frequency f_0 of 7.4 MHz and the initial phase T_d of 0 ns.

and $\hat{z}_2(f_0, T_{d2}, a_2; nT_s)$ do not overlap, which is described by the first and second subterms on the right-hand side of Eq. (4). Figure 10(b) shows an example when $\hat{z}_1(f_0, T_{d1}, a_1; nT_s)$ and $\hat{z}_2(f_0, T_{d2}, a_2; nT_s)$ overlap (echo was measured at beam position i in Fig. 11). The overlapped echoes from the LIB and MAB are automatically taken into consideration because the MSE $\alpha(f_0, T_{d1}, T_{d2}, a_1, a_2; \tau_1, \tau_2)$ is between the measured in vivo RF echoes $x(nT_s)$ and the echo model $z(f_0, T_{d1}, T_{d2}, a_1, a_2; nT_s)$ obtained using the sum of $\hat{z}_1(f_0, T_{d1}, a_1; nT_s)$ and $\hat{z}_2(f_0, T_{d2}, a_2; nT_s)$. The evaluation of the difference between the measured in vivo RF echoes $x(nT_s)$ and the sum of the echo models $\hat{z}_1(f_0, T_{d1}, a_1; nT_s)$ and $\hat{z}_2(f_0, T_{d2}, a_2; nT_s)$ is shown by the third subterm in Eq. (4). For the robust detection of LIB, the variance $\beta(nT_s \in L_1)$ in the region above the LIB echo (from T_0 to T_1) is calculated

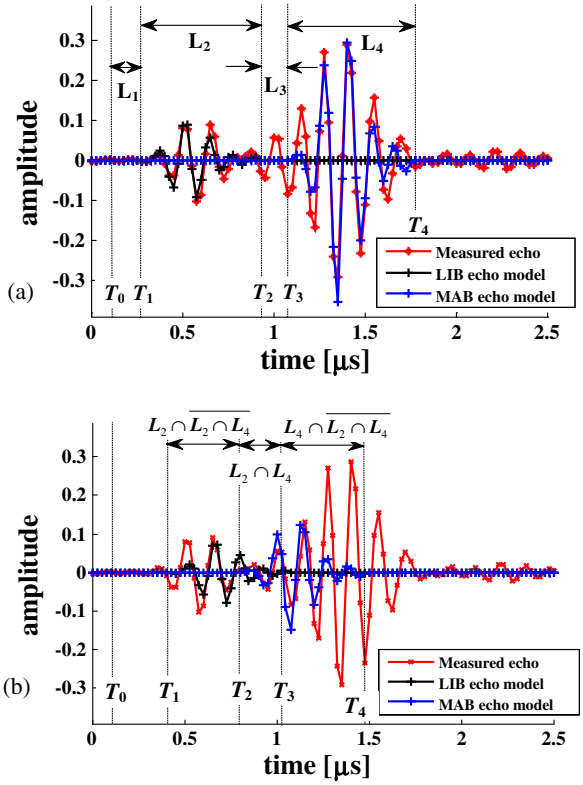

Fig. 10. (Color online) Measured signal at beam position i labeled in Fig. 11 and echo model in cases of (a) separated and (b) overlapped $\hat{z}_1(f_0, T_{d1}, a_1; nT_s)$ and $\hat{z}_2(f_0, T_{d2}, a_2; nT_s)$.

as shown by the second term on the right-hand side of Eq. (4), defined in Eq. (5). Note that T_0 is the starting point of the fitting process that is manually set. Since the magnitude of the echoes from the lumen is small, $\beta(nT_s \in L_1)$ is nearly zero. On the other hand, $\beta(nT_s \in L_1)$ increases when the LIB echo model is fitted to the MAB echo. Additionally, the variance $\beta(nT_s \in L_3)$ of the measured signals from T_2 to T_3 is added [Eq. (5)] when the echo models do not overlap. The variance $\beta(nT_s \in L_3)$ increases when the echo models are fitted with the echo from the tissue below the adventitia layer that is falsely detected. Therefore, the estimation of $\beta(nT_s \in L_3)$ could prevent the echo from below the adventitia layer from being detected. Overall, the misdetection of the LIB and MAB can be reduced by calculating such variances. Thereafter, the positions of the LIB and MAB echo models, $\hat{z}_1(f_0, T_{d1}, a_1; nT_s)$ and $\hat{z}_2(f_0, T_{d2}, a_2; nT_s)$, which give the minimum difference $\min\{\alpha(f_0, T_{d1}, T_{d2}, a_1, a_2; \tau_1, \tau_2)\}$ between the measured in vivo RF echo $x(nT_s)$ and echo model $z(f_0, T_{d1}, T_{d2}, a_1, a_2; nT_s)$ are determined as the optimum positions of the LIB and MAB.

3. Boundary Detection for In vivo Ultrasonic Data

In the in vivo measurement, the modified ultrasonic diagnostic equipment (ALOKA SSD-6500) was used. The right carotid artery of a healthy male at the age of 23 was scanned by a 10-MHz linear array transducer (ALOKA UST-5410), and the RF signals were sampled at 40 MHz at a 16-bit resolution. The electronic focus was set at 13.7 mm and the acoustic focus was at 20 mm. By applying the MSE method, as shown in Eq. (4), two restrictions were set in this detection procedure. First, the amplitude of detected MAB

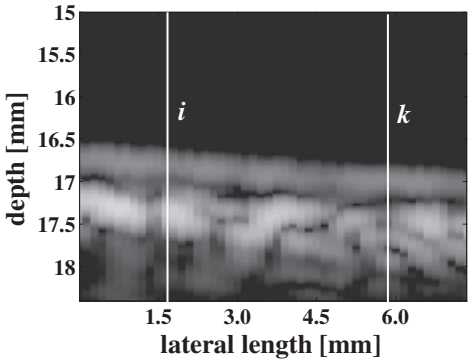

Fig. 11. B-mode image of posterior carotid arterial wall of healthy 23-year-old male.

should be larger than the amplitude of the detected LIB. Second, since the average IMT ranges from 0.39 to 0.62 mm for a healthy male aged between 17 and 63,[39] and the IMT varies from person to person, in this work, the range of $\tau_2 - \tau_1$ was scaled from 0.35 to 1.0 mm. Figure 11 shows the B-mode image of the posterior carotid arterial wall for a 7.5-mm-long short segment in the arterial longitudinal direction (with 150 μm beam spacing). The results of the evaluated MSE $\alpha(f_0, T_{d1}, T_{d2}, a_1, a_2; \tau_1, \tau_2)$ between the measured in vivo RF echoes $x(nT_s)$ and the echo model $\hat{z}(f_0, T_{d1}, T_{d2}, a_1, a_2; nT_s)$ for the beam position k labeled in the B-mode image of the posterior carotid arterial wall (Fig. 11) are shown in Fig. 12. Figure 12(a) represents the distribution of the minimum MSE $\min\{10\log_{10}\alpha(f_0, T_{d1}, T_{d2}, a_1, a_2; \tau_1, \tau_2)\}$ evaluated at the center frequencies of $f_0 = 7.4$ MHz for LIB and MAB echo models, for which the lowest minimum MSE $\min\{\alpha(f_0, T_{d1}, T_{d_2}, a_1, a_2; \tau_1, \tau_2)\}$ is determined at the initial phase $T_{d1} = 4$ ns of LIB and $T_{d2} = 24$ ns of MAB echo models. Focusing on the lowest $\min\{10\log_{10}\alpha(f_0, T_{d1}, T_{d2}, a_1, a_2; \tau_1, \tau_2)\}$ (with optimum phases and frequency of LIB and MAB echo models) of 21.2%, the positions of the LIB and MAB are indicated at point R, as shown in Fig. 12(b) of the MSE distribution $\{10\log_{10}\alpha(f_0, T_{d1}, T_{d2}, a_1, a_2; \tau_1, \tau_2)\}$. Note that the estimated $\min\{10\log_{10}\alpha(f_0, T_{d1}, T_{d2}, a_1, a_2; \tau_1, \tau_2)\}$ is between the normalized measured in vivo RF echo $x(nT_s)$ and the LIB and MAB echo models, $\hat{z}_1(f_0, T_{d1}, a_1; nT_s)$ and $\hat{z}_2(f_0, T_{d2}, a_2; nT_s)$. The positions of the LIB and MAB, which are the positions of the LIB and MAB echo models fitted with the measured in vivo RF echo at the minimum MSE $\min\{\alpha(f_0, T_{d1}, T_{d_2}, a_1, a_2; \tau_1, \tau_2)\}$, are shown in Fig. 12(c).

The MSE distributions $\{10\log_{10}\alpha(f_0, T_{d1}, T_{d2}, a_1, a_2; \tau_1, \tau_2)\}$, which are evaluated for the measured signal and the echo model without and with the variance $\beta(nT_s \in L_1)$, are presented in Figs. 13 and 14, respectively. To confirm the robustness of LIB detection by adding the variance $\beta(nT_s \in L_1)$, the distributions do not account for the variance $\beta(nT_s \in L_3)$. As shown in Fig. 13(a), the MSE without $\beta(nT_s \in L_1)$ appears to have more than one local minimum MSE other than region P. The local minimum in region R is similar to the global minimum in region P. Thus, a misdetection boundary would occur [Fig. 13(b)]. In contrast, as shown in Fig. 14(a), the MSE with $\beta(nT_s \in L_1)$ reduces the local minimum and focus into the LIB region. Considering the variance $\beta(nT_s \in L_3)$ in the MSE evalua-

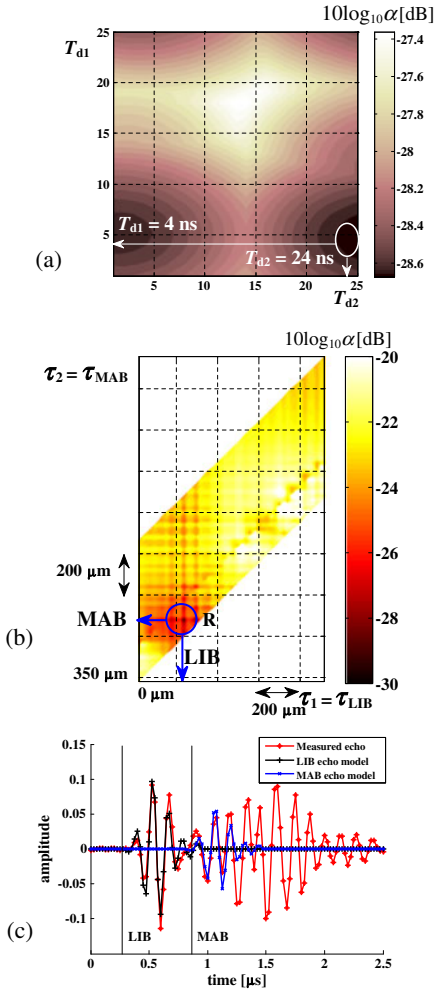

Fig. 12. (Color online) (a) Distribution of minimum MSE $\min\{\alpha(f_0, T_{d1}, T_{d_2}, a_1, a_2; \tau_1, \tau_2)\}$ at the frequency $f_0 = 7.4$ MHz of LIB and MAB echo models. (b) MSE distribution $\{10\log_{10}\alpha(f_0, T_{d1}, T_{d2}, a_1, a_2; \tau_1, \tau_2)\}$ indicating the positions of LIB and MAB at point R. (c) Estimated minimum MSE $\min\{\alpha(f_0, T_{d1}, T_{d_2}, a_1, a_2; \tau_1, \tau_2)\}$ of 21.2% between the measured in vivo RF echo at beam position k and the LIB and MAB echo models.

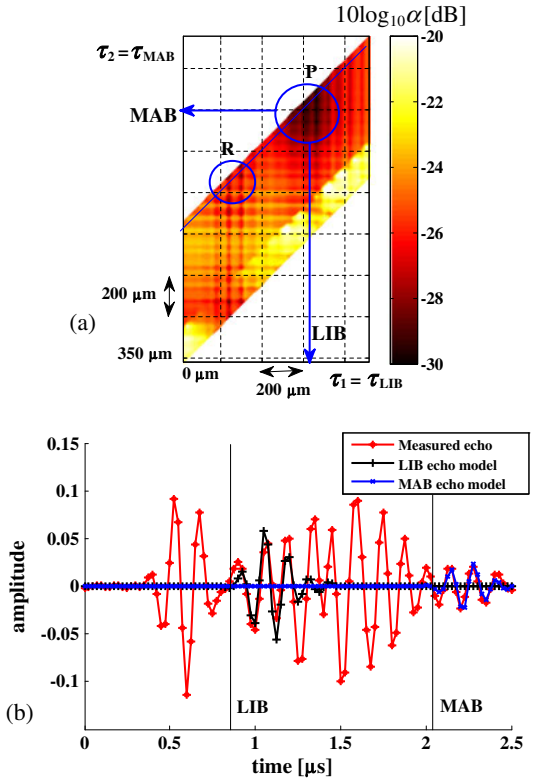

Fig. 13. (Color online) (a) MSE distributions $\{10\log_{10}\alpha(f_0, T_d; \tau_1, \tau_2)\}$ evaluated for measured signal and echo model without the variance $\beta(nT_s \in L_1)$. (b) Result of fitting of measured signal and echo model without the variance $\beta(nT_s \in L_1)$.

tion, the MAB echo model is fitted closer to the LIB region, as shown in Fig. 12(c). Meanwhile, the MAB echo model is fitted at the position with the distance of L_3 from the LIB echo model [Fig. 14(b)] when the variance $\beta(nT_s \in L_3)$ is not considered in the MSE evaluation. These results verified that the estimation of the $\beta(nT_s \in L_3)$ could prevent the echo from the tissue below the adventitia layer from being detected. Therefore, the misdetection of the LIB and MAB can be reduced by calculating such variances.

4. Discussion

In the present study, the template matching technique of our proposed automated method has been improved to detect the boundaries of the intima-media complex (IMC) more accurately. We also considered the echo model using the received pulse estimated from the transmitted wave measured using a hydrophone, instead of referring the echo from a point scatterrer. As explained in Sect. 2.2, the excitation signal $x(t)$ was assumed to be an impulse. However, the actual signal was a rectangular pulse with a width of half the wavelength. In such a case, the frequency

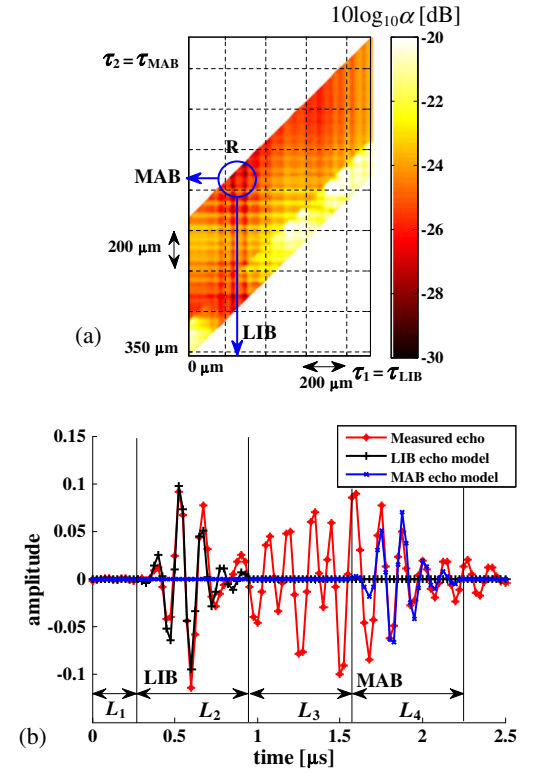

Fig. 14. (Color online) (a) MSE distributions $\{10\log_{10}\alpha(f_0, T_d; \tau_1, \tau_2)\}$ evaluated for measured signal and echo model with the variance $\beta(nT_s \in L_1)$. (b) Result of fitting of measured signal and echo model with the variance $\beta(nT_s \in L_1)$.

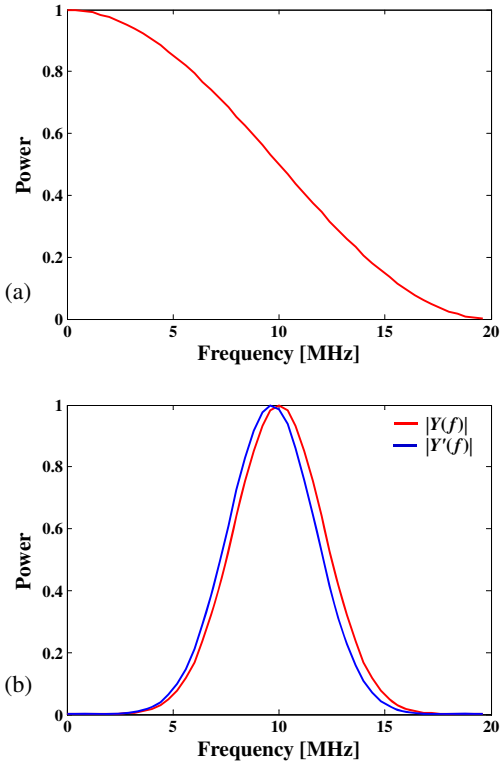

Fig. 15. (Color online) (a) Power spectrum $|X(f)|^2$ of a rectangular pulse with a pulse length of half the wavelength. (b) Power spectra $|Y(f)|^2$ and $|Y'(f)|^2$.

spectra $Y(f)$ and $H(f)$ of the transmitted ultrasonic pulse $h(t)$ measured with a hydrophone and received pulse $y(t)$ are expressed as follows:

$$H(f) = G(f)X(f), \tag{6}$$

$$Y(f) = \{G(f)\}^2 X(f) = \frac{\{H(f)\}^2}{X(f)}. \tag{7}$$

In the present study, the estimated $Y'(f)$ of the received pulse $Y(f)$ was defined as $\{H(f)\}^2$. Therefore, the bandwidth of $Y'(f)$ is narrower than $Y(f)$ owing to the over consideration of $X(f)$. Let us explain the effect of the over consideration of $X(f)$ below. Figure 15(a) shows the power spectrum [corresponding to $|X(f)|^2 = f_0^2[1 - \cos(\pi f/f_0)]/(\pi^2 f^2)$] of a rectangular pulse with a length of half the wavelength at a center frequency $f_0 = 10$ MHz, simulating the excitation signal $x(t)$. For simplicity, in this explanation, the amplitude spectrum $|H(f)|$ of the transmitted wave $h(t)$ was assumed to be Gaussian ($= \exp[-(f - f_0)^2/\sigma^2]$, $\sigma = 3$ MHz in Fig. 15). Figure 15(b) shows $|Y(f)|^2 = |\{H(f)\}^2/X(f)|$ and $|Y'(f)|^2 = |\{H(f)\}^2|$. As can be seen in Fig. 15(b), the over consideration of $X(f)$ shifted the center frequency and decreased the bandwidth (width at half maximum) by 2.6%. The shift of the center frequency can be compensated by stretching or compressing the model signal in the proposed method. There should be a change in waveform owing to the decrease in the bandwidth. However, the change in bandwidth would be a few percent (2.6%) as described above and it can be assumed to be negligible.

For the evaluation of the results, we compared the boundaries in a few beams obtained by our improved technique of the proposed automated method, the previous method, and the manual method. Figures 16(a) and 16(b)

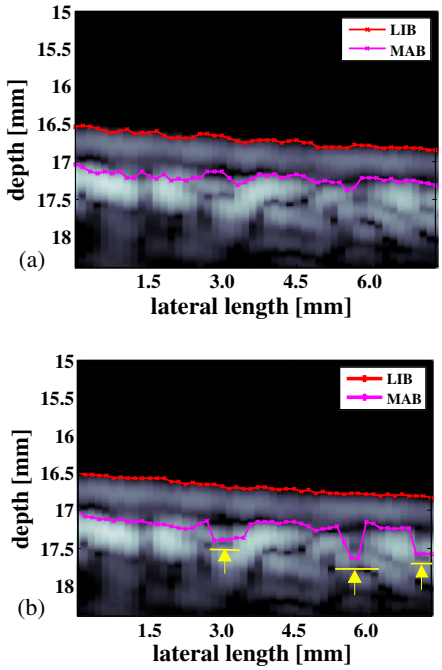

Fig. 16. (Color online) B-mode image of detected boundaries of the posterior carotid arterial wall by (a) the improved template matching technique of the proposed method and (b) the previous method.

show boundaries detected by the improved template matching technique of the proposed method and those by the previous method, respectively. From these results, at some beam positions [marked by arrows with yellow lines in Fig. 16(b)], the boundaries estimated by the improved technique differ from those estimated by the previous one. For all the analyzed beams, only (4.8–27.5%) of $\min\{\alpha(f_0, T_{d1}, T_{d2}, a_1, a_2; \tau_1, \tau_2)\}$ convinces us that the echo model used in this study is in very good agreement with the measured in vivo RF echo. Moreover, the average IMTs for a 7.5-mm-long short segment in the arterial longitudinal direction calculated by the improved technique and that by the previous one are 502 ± 61 and $558 \pm 120\,\mu$m, respectively, showing a decrease in the standard deviation. Thus, the proposed method yields better results than the previous method and leads to more accurate boundary detection. From the manual method of boundary detection, as shown in Fig. 17, that was carried out by observing the B-mode image, the average IMT for a 7.5-mm-long short segment in the arterial longitudinal direction was $504 \pm 65\,\mu$m. This result shows that the improved technique achieve a smaller difference in the estimated average IMT from that by manual method (only 0.4% difference) compared with the average IMT obtained by the previous method (10.7% difference). However, since the manual method is lacks reproducibility and depends on the operator, the comparison between the result obtained by the automated method and that by the manual method is not satisfactory for evaluation. We found that it is difficult to evaluate the results obtained in the present study since the true values are not provided in the in vivo measurement. Hence, the accuracy evaluation of the improved technique of our proposed method should be further investigated. Furthermore, at a few beams, small distortions of MAB are observed. This could be due to the

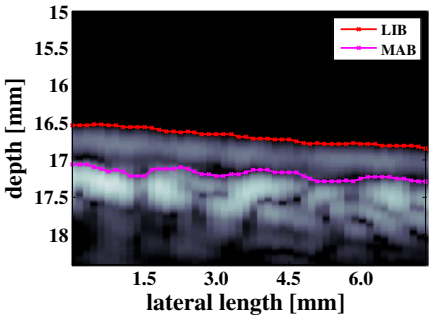

Fig. 17. (Color online) B-mode image with detected boundaries of the posterior carotid arterial wall obtained by the manual method.

interference of ultrasound echoes caused by tissue scatterers spaced closer together than the duration of ultrasonic pulses. In this study, the wavelength of an ultrasound wave was 150 μm at 10 MHz. The adventitia layer, which consists of mostly of tissues such as bundles of collagen fibers,[38] is smaller than the wavelength of ultrasound (tissue cells are 10–20 μm thick and 15–50 μm high).[40] The ultrasound wave that is emitted to such small structures scatters and returns to the transducer through multiple pathways. Thus, the echo that returns to the transducer is no longer coherent. It is instead the sum of a number of echoes that produces a complex pattern of constructive and destructive interference. Boundary detection would be influenced by such interference. Furthermore, more than one scatterers would exist in the adventitia layer owing to the bundles of collagen fibers, compared with the intima layer, which consists of a single layer of endothelium cells. Thus, the adventitia layer produces multiple interfaces that could be misdetected as MAB. In a future work, to improve the detection of MAB by considering the multiple interfaces produced in the adventitia layer, multiple echo models should be employed when fitting with the echo from the MAB instead of an echo model. However, the waveform of the measured echo in this case should also be further analyzed to obtain a better result. In summary, the results obtained in the present study using the improved proposed method showed an advantage for the automatic estimation of the IMT of the carotid arterial wall, and it would be useful for the diagnosis of early-stage atherosclerosis.

5. Conclusions

In this study, using the proposed template matching technique, we automatically estimated the boundary positions of IMT in the posterior wall of the carotid artery of a 7.5-mm-long short segment in the arterial longitudinal direction. The technique realized more accurate MAB detection. Moreover, for the accurate detection of the LIB and MAB, the frequency and phase of the echo model were considered when fitting with the measured echo. It was observed that the average IMT obtained by the improved technique in the present study was 502 ± 61 μm, showing a decrease in standard deviation compared with the average IMT of 558 ± 120 μm obtained by the previous method. Thus, the method employed in the present study yields more accurate results than the previous method and leads to accurate boundary detection.

1) S. Mendis, P. Puska, and B. Norrving: *Global Atlas on Cardiovascular Disease Prevention and Control* (World Health Organization, Geneva, 2011) p. 3.
2) S. S. Anand, S. Yusuf, and V. Vuksan: Lancet **356** (2000) 279.
3) M. Tatsukawa, Y. Sawayama, N. Maeda, K. Okada, N. Furusyo, S. Kashiwagi, and J. Hayashi: Atherosclerosis **172** (2004) 337.
4) A. Lakka, H. Lakka, R. Salonen, G. A. Kaplan, and J. T. Salonen: Atherosclerosis **154** (2001) 497.
5) J. Gariepy, J. Salomon, N. Denarie, F. Laskri, J. L. Megnien, J. Levenson, and A. Simon: Arterioscler. Thromb. Vasc. Biol. **18** (1998) 584.
6) J. Gariepy, M. Massonneau, J. Levenson, D. Heudes, and A. Simon: Hypertension **22** (1993) 111.
7) E. de Groot, G. K. Hovingh, A. Wiegman, P. Duriez, A. J. Smit, J.-C. Fruchart, and J. J. P. Kastelein: Circulation **109** (2004) III-33.
8) J. N. Cohn, A. A. Quyyumi, N. K. Hollenberg, and K. A. Jamerson: Circulation **109** (2004) IV-31.
9) W. Stanford, B. H. Thompson, and R. M. Weiss: Am. J. Roentgenol. **161** (1993) 1139.
10) P. Pignoli, E. Tremoli, A. Poli, P. Oreste, and R. Paoletti: Circulation **74** (1986) 1399.
11) K. Yamamoto, M. Yamamoto, N. Yamamoto, and M. Aoyagi: Connective Tissue **34** (2002) 317.
12) E. W. Raines and R. Ross: Br. Heart J. **69** (1993) S30.
13) R. Ross: New Engl. J. Med. **340** (1999) 115.
14) D. H. O'Leary, J. F. Polak, R. A. Kronmal, T. A. Manolio, G. L. Burke, and S. K. Wolfson: New Engl. J. Med. **340** (1999) 14.
15) M. L. Bots, A. Hofman, P. T. V. M. D. Jong, and D. E. Grobbee: Ann. Epidemiol. **6** (1996) 147.
16) D. Baldassarre, M. Amato, A. Bondioli, C. R. Sirtori, and E. Tremoli: Stroke **31** (2000) 2426.
17) S. M. Ellis, R. P. Naoumova, C. K. Neuwirth, R. Eckersley, D. O. Cosgrove, G. R. Thompson, and P. S. Sidhu: Ultrasound Med. Biol. **33** (2007) 1029.
18) I. M. Graf, F. H. B. M. Schreuder, J. M. Hameleers, W. H. Mess, R. S. Reneman, and A. P. G. Hoeks: Ultrasound Med. Biol. **35** (2009) 955.
19) P. H. Davis, J. D. Dawson, M. B. Blecha, R. K. Masterbergen, and M. Sonka: Ultrasound Med. Biol. **36** (2010) 560.
20) A. D. M. van Swijndregt, S. H. K. The, E. J. Gussenhoven, C. T. Lancee, H. Rijsterborgh, E. de Groot, A. F. W. van der Steen, N. Bom, and R. G. A. Ackerstaff: Ultrasound Med. Biol. **22** (1996) 1007.
21) A. Poli, E. Tremoli, A. Colombo, M. Sirtori, P. Pignoli, and R. Paoletti: Atherosclerosis **70** (1988) 253.
22) J. Wikstrand: Clin. Physiol. Funct. Imaging **27** (2007) 341.
23) M. R. de Groot and J. D. Banga: Eur. J. Vasc. Surg. **8** (1994) 257.
24) J. F. Polak, L. C. Funk, and D. H. O'Leary: J. Ultrasound Med. **30** (2011) 915.
25) L. Saba, R. Sanfilippo, R. Montisci, and G. Mallarini: Am. J. Neuroradiol. **31** (2010) 1758.
26) L. Saba, R. Sanfilippo, R. Montisci, J. S. Suri, and G. Mallarini: Am. J. Neuroradiol. **34** (2013) E13.
27) L. Boussel, A. Serusclat, M. R. Skilton, F. Vincent, S. Bernand, P. Moulin, D. Saloner, and P. C. Douek: J. Cardiovasc. Magn. Resonance **9** (2007) 771.
28) H. Yanai, H. Yoshida, Y. Tomono, and N. Tada: Q. J. Med. **100** (2007) 253.
29) V. Savithri and S. Purushothaman: Int. J. Adv. Computer Sci. Appl. **1** (2010) 78.
30) Q. Liang, I. Wendelhag, J. Wikstrand, and T. Gustavsson: IEEE Trans. Med. Imaging **19** (2000) 127.
31) C. P. Loizou, C. S. Pattichis, M. Pantziaris, T. Tyllis, and A. Nicolaides: Med. Biol. Eng. Comput. **45** (2007) 35.
32) R. Rocha, A. Campilho, J. Silva, E. Azevedo, and R. Santos: Image Vision Comput. **28** (2010) 614.
33) S. Golemati, J. Stoitsis, E. G. Sifakis, T. Balkizas, and K. S. Nikita: Ultrasound Med. Biol. **33** (2007) 1918.
34) T. Kaneko, H. Hasegawa, and H. Kanai: Jpn. J. Appl. Phys. **46** (2007) 4881.
35) K. Ikeshita, H. Hasegawa, and H. Kanai: Jpn. J. Appl. Phys. **50** (2011) 07HF08.
36) N. Ibrahim, H. Hasegawa, and H. Kanai: Jpn. J. Appl. Phys. **51** (2012) 07GF07.
37) L. Fan, P. Santago, W. Riley, and D. M. Herrington: Ultrasound Med. Biol. **27** (2001) 399.
38) G. A. Holzapfel and T. C. Gasser: J. Elasticity **61** (2000) 1.
39) A. Simon, J. Gariepy, G. Chironi, J. L. Megnien, and J. Levenson: J. Hypertension **20** (2002) 159.
40) Y. Uehara, I. Saito, T. Kushiro, and F. Nakamura: *Hitomede-Wakaru Kekkan Shogai* (Vascular Disorders at a Glance) (MEDSI, Tokyo, 1995) [in Japanese].